PAPER

Structural, optical and conductivity properties in tetragonal BaTi$_{1-x}$Co$_x$O$_3$ (0≤ x ≤0.1)

L. T. H. Phong,[a] N. T. Dang,[bc] N. V. Dang,[di] Van-Quynh Nguyen,[e] D. H. Manh, [a]
P. H. Nam,[af] L. H. Nguyen[gh] and P. T. Phong [*gh]

This work investigates the structure, optical and electrical conductivity properties of BaTi$_{1-x}$Co$_x$O$_3$ (0≤ x ≤0.1) ceramics prepared by the hydrothermal method. The X-ray diffraction and Raman scattering analysis demonstrates that the prepared samples have a single-phase tetragonal structure with *P4mm* symmetry. The UV-vis diffuse reflectance spectrum confirms the influence of Co concentration on the direct optical band gap of BaTi$_{1-x}$Co$_x$O$_3$ ceramics. The optical band gap shifts from 3.14 eV to 3.44 eV as the Co concentration increases from 0 to 0.1. The dielectric constant increases with the depletion of frequency according to the Maxwell–Wagner and Koops model. The AC conductivity *versus* frequency curve indicates that the conduction mechanism is determined by using the correlated barrier hopping (CBH) model. The Cole–Cole plot of the complex impedance was investigated for the prepared samples. The compounds showed dielectric relaxation of the non-Debye type.

1. Introduction

Barium titanate (BaTiO$_3$) is a common lead-free ferroelectric material that has excellent insulating, dielectric, and ferroelectric properties; it is widely utilized to fabricate electronic components, such as multilayer ceramic capacitors (MLCCs), positive-temperature coefficient thermistors, piezoelectric transducers, and electro-optic devices.[1–3] BaTiO$_3$ (BTO) undergoes four successive phase transitions due to distortion of the TiO$_6$ octahedra with increasing temperature: from rhombohedral to orthorhombic at −90 °C, from orthorhombic to tetragonal structure at 5 °C, from tetragonal to cubic phase at 130 °C, and from cubic to a hexagonal phase (6H- BTO) at 1460 °C[4] These phase transitions are accompanied by the appearance of large anomalies of the relative permittivity (ε_r) and the maximum ε_r value of 10 000 at Curie temperature (T_C = 130 °C).[5]

Above the T_C temperature, BTO is no longer ferroelectric, and its ε_r decreases according to the empirical Curie–Weiss law. The temperature dependence of ε_r is affected by structural phase transitions. This phenomenon typically is undesirable for most technological applications, especially for MLCCs.[6] To reduce the temperature dependence of ε_r in BTO-based ceramics and broaden its applications, doping with different ions is one of the most judicious strategies to approach. Nakayama and Katayama-Yoshida[7] predicted the stability of magnetic structures of BaTiO$_3$ doped with transition metals (Sc, V, Cr, Mn, Fe, Co, Ni, Cu) through *ab initio* total energy calculations. They showed that although the ground state of actual Co-doped BaTiO$_3$ was ferromagnetic, the Curie temperature could not reach as high as expected. In another report, Yang *et al.*[8] observed the paramagnetic behavior of BaTi$_{1-x}$Co$_x$O$_3$ samples (0.05≤ x ≤0.25). They believed that the system of isolated paramagnetic centers of Co^{4+} ions produced a paramagnetic state in the samples. It was in good agreement with the work reported by Liu *et al.*[9] Meanwhile, Phan *et al.*[10] observed the co-existence of paramagnetic and weak ferromagnetic behavior in BaTi$_{1-x}$Co$_x$O$_3$ samples (0.0< x ≤0.1). Using X-ray absorption spectra data, they explained that the paramagnetic nature was due to isolated Co^{2+} and Co^{3+} centers, in which the Co^{3+} ions played a dominant role in enhancing the paramagnetic behavior. However, these results differ from the ferromagnetic characteristic reported previously on BaTi$_{0.98}$Co$_{0.02}$O$_3$ epitaxial thin films[11] and Co-doped BaTiO$_3$ thin films.[12] As such, ferromagnetism in BaTi$_{1-x}$Co$_x$O$_3$ materials depends not only on impurities and doping levels but also on crystal defects and sample forms and their dimensions (*i.e.*, thin films, nanostructures, or single-crystal and polycrystalline bulks). Sample

ᵃInstitute of Materials Science, Vietnam Academy of Science and Technology, Hanoi, Vietnam

ᵇInstitute of Research and Development, Duy Tan University, 550000, Da Nang, Vietnam

ᶜFaculty of Natural Sciences, Duy Tan University, 550000, Da Nang, Vietnam

ᵈDepartment of Physics and Technology, Thai Nguyen University of Science, Thai Nguyen City, Vietnam

ᵉUniversity of Science and Technology of Hanoi (USTH), Vietnam Academy of Science and Technology, Ha Noi, Vietnam

ᶠGraduate University of Science and Technology, Vietnam Academy of Science and Technology, Hanoi, Vietnam

ᵍLaboratory of Magnetism and Magnetic Materials, Science and Technology Advanced Institute, Van Lang University, Ho Chi Minh City, Vietnam. E-mail: phamthanhphong@vlu.edu.vn

ʰFaculty of Technology, Van Lang University, Ho Chi Minh City, Vietnam

ⁱHong Duc University, Thanh Hoa, Vietnam

synthesis and/or processing conditions strongly influence the structural and magnetic properties of $BaTi_{1-x}Co_xO_3$. It is similar to circumstances occurring in dilute magnetic semiconductors.[13] Interestingly, the Co doping at the Ti site may cause BTO to form a polymorphic phase. Yang *et al.*[8] reported that $BaTi_{1-x}Co_xO_3$ ($0.0< x \leq 0.25$) samples prepared by the hydrothermal method exhibit a pure tetragonal structure, but it has a hexagonal phase as the major phase in other studies.[14-19] Li *et al.*[15] observed that the tetragonal structure of $BaTi_{1-x}Co_xO_3$ ($0.01\leq x \leq 0.20$) samples only exist at $x \leq 0.03$, and it is transformed gradually to a hexagonal structure when Co content increases up to the value of 0.05. Phan *et al.*[10] observed that tetragonal–hexagonal transformation occurs at $x = 0.01$ in $BaTi_{1-x}Co_xO_3$ ($0.0< x \leq 0.1$). However, a few works paid attention investigating the optical, dielectric characteristics, and conductivity mechanism of Co-doped BTO. In general, study of electrical conductivity in ferroelectrics is important to obtain in-depth understanding of related physical properties, such as piezoelectricity and thermoelectricity. Moreover, polarization strategies depend on the order and nature of electrical conductivity in these materials.[8]

The conventional method for fabrication of transition metal-doped $BaTiO_3$ ceramic is the solid–state reaction of carbonate and oxide raw materials at high temperatures, typically around 1100 °C. After milling, the particle sizes are 1–2 μm in diameter. Most actual engineering applications require a development of material with high density and high dielectric constants; in this regard, new fabrication methods have been explored. Among others, chemical approaches to fabricate the transition metal-doped $BaTiO_3$ powder have more advantages. It has been chosen by many research groups to prepare materials.[15,20,21] The hydrothermal method is a low-cost, low-temperature, and large-scale technology that has been used to prepare homogeneous particles of various shapes and sizes in the nanoscale.[22] Moreover, powders produced by this technique have been evidenced to be highly reactive towards sintering,[23] therefore, the phase structure of powders obtained by hydrothermal method is stable during sintering at a high temperature. Zhu *et al.*[24] reported that hydrothermally synthesized tetragonal BTO nanoparticles have a better sintering behavior, higher density, and higher dielectric constant than cubic-phase ones prepared by other methods.

In this study, the $BaTi_{1-x}Co_xO_3$ ($0.0< x \leq 0.1$) ceramic were synthesized using hydrothermal method combined with annealing temperature method. The structure of the products was characterized in detail. In addition, the effects of the amount of Co on the optical, dielectric properties and conductivity of Co-doped $BaTiO_3$ pellets were investigated.

2. Experimental details

2.1 Synthesis of Co-doped $BaTiO_3$ ceramic

$BaTi_{1-x}Co_xO_3$ (BTCO) ceramic (with $x = 0.00, 0.02, 0.04, 0.06, 0.08$ and 0.10) were synthesized by hydrothermal method. Reagents of TiO_2 (~99.9%), $Ba(OH)_2 \cdot 8H_2O$ (99.9%), $Co(NO_3)_2 \cdot 6H_2O$ (99.9%), and H_2O_2 (30%) purchased from Sigma-Aldrich. Chemicals were used as raw materials. A mixture of TiO_2,

$Ba(OH)_2 \cdot 8H_2O$, and $Co(NO_3)_2 \cdot 6H_2O$ were prepared with distilled water. The droplets of NaOH (10 M) were added gradually into the as-prepared mixture to control the pH of 13. The resulted mixture was then stirred for 60 minutes to obtain a homogeneous solution. A Teflon-lined autoclave with 100 mL capacity filled by 80% of its volume was used. The solution was maintained in the autoclave at 180 °C for 20 h. The temperature was increased at a rate of 5 °C min^{-1}. It was subsequently cooled down to room temperature naturally. After the reaction, the powders were filtered, washed thoroughly in diluted acetic acid and distilled water afterward until its pH reached neutral. It was then dried in oven at 80 °C for 10 h. The obtained powder was pressed into circular pellets of 13 mm in diameter and 1 mm in thickness under a pressure of 5 tons cm^{-2}. The pellets were then sintered at 1100 °C for 20 h in air. The pellets were rapidly cooled to room temperature to keep the structure at the annealing temperature.[25]

2.2 Characterization of $BaTi_{1-x}Co_xO_3$

2.2.1 X-ray diffraction. The structure and phase of the samples were identified by powder X-ray diffraction (XRD, Bruker D8 Advance instrument operating at 35 kV and 30 mA) using Cu Kα radiation ($\lambda = 1.5406$ Å). Rietveld refinement data were collected from $20°$ to $80°$ (2θ) with a step length of $0.02°$ and a fixed counting time of 7 s per step. The structural parameters, phase fractions, and fitting parameters were refined using the FullProf program.[26]

2.2.2 Scanning electron microscopy. The surface morphology of the samples was characterized by Hitachi S-4800 field-emission scanning electron microscope (FESEM). The energy-dispersive X-ray spectroscopy (EDX) was used to evaluate the powdered samples of various elemental compositions (*i.e.* $x = 0.0$, $x = 0.04$, and $x = 0.10$) deposited on a Si wafer.

2.2.3 UV-vis-NIR spectroscopy. Optical absorbance of the prepared powders was recorded using Cary 5000 UV-Vis-NIR double beam spectrophotometer (Agilent Technologies, Santa Clara, USA) equipped with an integrating sphere attachment. $BaSO_4$ was used as the background, and scanning was conducted over the 300–600 nm range of wavelength.

2.2.4 Raman spectroscopy analysis. The Raman spectra of the sintered $BaTi_{1-x}Co_xO_3$ pellets were recorded in backscattering geometry with a Raman spectrometer (Jobin-Yvon Lab RAM HR800) at room temperature. Laser of 532 nm wavelength and 17 mW power was used to characterize the samples. Laser beam of 1.0 mm in radius was focused on the sample's surface by an objective lens with a magnification of $50\times$. All spectra were taken in the wavenumber region from 300 cm^{-1} to 800 cm^{-1}.

2.2.5 Dielectric analysis. The dielectric properties of the prepared ceramics at room temperature were evaluated using broadband dielectric spectrometer (HP 4192A) at amplitude of 0.5 V with frequency of 1 Hz to 0.1 MHz controlled by a computer. The pellet-shaped samples were polished, and silver paste was applied to both sides of each plate connected to the spectrometer with special cables for dielectric measurements. Data were analyzed by ZSimpWin software.

3. Results and discussion

3.1 Structural analysis

Fig. 1 presents the experimental diffractograms and the positions of Bragg lines of the samples with different Co contents. The analysis of the Bragg profiles in comparison to the Rietveld refinements with possible structural models shows that all the peaks of the spectrum are perfectly indexed in the tetragonal *P4mm* symmetry structure (JCPD 81-2203). No impurity phases observed from the XRD patterns confirms all characterized samples have the single tetragonal structure within the detection limit of the measurement. This observation of tetragonal phase in our samples is different from previous reports on the observation of hexagonal phase.[16–19] However, it is in good agreement with the findings of Yang *et al.*[15] about the existence of the tetragonal phase in $BaTi_{1-x}Co_xO_3$ nanoparticles ($0.0 \le x \le 0.25$) prepared by the hydrothermal method at temperatures below 200 °C. Other authors found the tetragonal–hexagonal phase transformation in $BaTi_{1-x}Co_xO_3$ samples.[9,10,16,27] The divergences in the obtained structure of $BaTi_{1-x}Co_xO_3$ originate from impurity type, annealing temperature, and sample processing condition, which affect the formation of oxygen vacancies. When the number of oxygen vacancies becomes too high, the tetragonal structure is distorted and be transformed into the hexagonal phase.[20] In the present study, the samples with no observation of the hexagonal phase indicate that the distortions induced by oxygen vacancies are accommodated by the tetragonal structure; this phenomenon is an advantage of hydrothermal method over other synthesis methods. The refined structural parameters of the samples are summarized in Table 1. The experimentally observed and theoretically calculated X-ray pattern profiles display a minor difference shown by a wine line ($Y_{Obs} - Y_{Calc}$). The fitting parameters (R_B and R_p) suggest that the refinement results are very satisfactory. After carefully repeating the refinement, the R_p values for all samples are below 5.0%. The lattice parameter a slight increases with increasing amount of Co doped and is close to that of bulk T-BTO ($a = 3.998$ Å[28]) for $x = 0.10$ sample; however, the lattice parameter c slightly decreases. Moreover, the tetragonality ratio (c/a) decreases with increasing Co concentration. The opposite change trends of a and c lattice parameters lead to the linear increase in the unit cell volume with increasing doping level.[29,30] The increase in the unit cell volume can be due to the significantly larger ionic radius of Co than that of the Ti^{4+} ion. When the coordination number is 6, the Co ion can exist in the samples with different spin and oxidation states with different ionic radii: Co^{2+} (low spin, 0.65 Å), Co^{2+} (high spin, 0.745 Å), Co^{3+} (low spin, 0.545 Å), Co^{3+} (high spin, 0.61 Å), and Co^{4+} (high spin, 0.53 Å). The ionic radius of Ti^{4+} (0.605 Å) is the same as that of Co^{3+} (high spin),[31] so the substitution of Co^{3+} (high spin) for Ti^{4+} did not affect the change in the unit cell volume. The substitution of Co^{2+}, which has a larger ionic radius, for Ti^{4+}
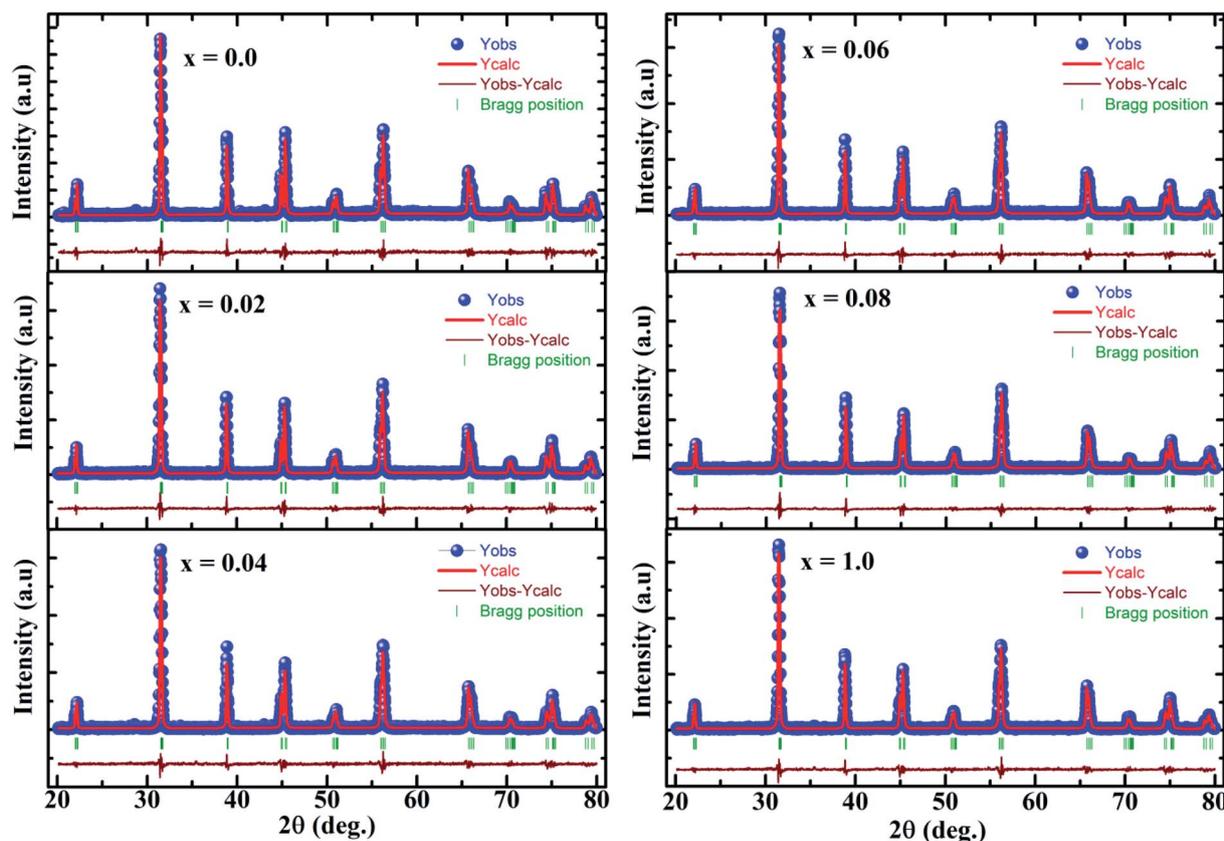

Fig. 1 Refined X-ray diffraction patterns of $BaTi_{1-x}Co_xO_3$ samples. The solid blue circle represents the observed profiles, the continuous red line represents refined profiles, and the wine line represents different profiles. The thick green markers correspond to Bragg position.

Table 1 Refined structural parameters, characteristic bond lengths and angles of $BaTi_{1-x}Co_xO_3$ compounds. In the tetragonal $P4mm$ structure, atoms are located at following crystallographic sites Ba 1a (0, 0, 0), Ti/Co 1b (1/2, 1/2, z), O1 1b (1/2, 1/2, z), and O2 2c (1/2, 0, z)

x (Co)	0	0.02	0.04	0.06	0.08	0.10
$a = b$ (Å)	3.9926(2)	3.9948(2)	3.9954(2)	3.9969(2)	3.9972(2)	3.9971(2)
c (Å)	4.0331(3)	4.0287(3)	4.0282(3)	4.0257(3)	4.0252(3)	4.0251(3)
V (Å^3)	64.291(7)	64.293(6)	64.304(7)	64.311(7)	64.312(6)	64.307(7)
c/a	1.0101(4)	1.0084(8)	1.0082(1)	1.0072(1)	1.0070(0)	1.0070(0)
Ti/Co: z	0.513(8)	0.529(4)	0.527(4)	0.538(3)	0.538(3)	0.542(3)
O1: z	0.008(47)	0.012(26)	0.011(27)	0.022(19)	0.015(22)	0.016(22)
O2: z	0.461(14)	0.454(10)	0.465(12)	0.460(11)	0.460(11)	0.466(13)
R_B (%)	8.52	9.06	8.46	9.22	9.36	10.1
R_p (%)	4.26	4.43	3.92	4.60	4.33	4.85

increases the lattice parameters, while the substitution of Co^{3+} (low spin) and Co^{4+} (high spin), which have smaller ionic radius, decreases the lattice parameters. The change in the lattice parameters induced by Co doping can be interpreted in terms of possible replacement of Co^{2+} ions rather than Co^{3+} and Co^{4+} ions at Ti^{4+} sites. This finding matches with the slight shift of the diffraction peak at $2\theta = 31.5°$ to lower angle with increasing Co content. However, Padilla-Campos et al.[29] believed that Co^{2+} ions simultaneously replace Ba^{2+} and Ti^{4+} sites, resulting in small lattice distortion; this phenomenon would explain the shift to lower 2θ values. Contrary to this, Ma et al.[32] theoretically predicted that the Co atoms prefer to occupy the Ti site of $BaTiO_3$ by formation energy. The occupation of Ti sites by the Co^{2+} ions can generate oxygen vacancies to maintain the charge balance. If the oxygen vacancies are mostly located along the c-axis, then the decrease in the c lattice parameter would be larger. This characteristic is well-known among perovskite structures with oxygen vacancies.[33] The different ionic radius between Co and Ti can cause strain in the crystal, which is confirmed by the broadening diffraction line profile of the host lattice. If this strain is sufficiently large, then the CoO_6/TiO_6 octahedra tilt and result in structural phase transition. Therefore, the determining the lattice strain from the XRD peaks can provide evidence for the tetragonal crystalline phase stabilization in samples. Lattice strain (ε) can be determined using the following expression[34]

$$\varepsilon = \frac{\beta_{2\theta}}{4 \tan \theta} \qquad (1)$$

where $\beta_{2\theta}$ and θ are the full width at half maximum (FWHM) of individual diffraction peaks and Bragg's angle, respectively. The average ε value for each sample was obtained by calculation for all diffraction peaks. Fig. 2 depicts the variation in the mean lattice strain as a function of Co concentration. The lattice strain value is within 0.32% to 0.37% with increasing Co concentration. The slight change in strain implies that they are not sufficiently high to produce structural phase transitions in the studied samples.[20] In addition, the Raman scattering results show evidence of the tetragonal phase in $BaTi_{1-x}Co_xO_3$ samples.

3.2 Raman analysis

Cubic $BaTiO_3$ inherently has no Raman active modes, whereas the tetragonal $P4mm$ symmetry is expected to have eight Raman active modes, namely, $3A_{1g} + B_{1g} + 4E_g$.[35] Fig. 3 shows the Raman

spectra of the samples. The Raman spectrum of pure $BaTiO_3$ ($x = 0$) reveals sharp band at 305 cm^{-1}; an interference dip at 180 cm^{-1}, which appears as a signature of a long-range ferroelectric phase;[36] and three broad bands at 260 cm^{-1} [A_1(TO)], 515 cm^{-1} [A_1(TO)], and 720 cm^{-1} [A_1(LO)]. The Raman scattering bands at 305 and 720 cm^{-1} are assigned to the characteristic peaks of tetragonal $BaTiO_3$.[37] These results are in good agreement with the published literature for the Raman spectrum of tetragonal $BaTiO_3$.[38,39] A low concentration of Co has a dramatic impact on the observable modes. In particular, the peak at $\sim$305 cm^{-1} has reduced sharpness in the $x = 0.02$ sample and starts to broaden and overlap with the peak at $\sim$260 cm^{-1} in the $x \geq 0.04$ sample. The dip at 180 cm^{-1} in pure $BaTiO_3$ is affected by small amounts of Co and disappears at $x = 0.04$, indicating the start of the disruption of the long-range ferroelectric order of the sample.[36] The peaks at 260 and 305 cm^{-1} broadened and collapsed with increasing x; therefore, the Raman spectra of the $x \geq 0.04$ samples were deconvoluted using Lorentzian functions. The result shows four vibration modes at 260, 305, 515, and 720 cm^{-1}. The peak at 515 did not shift as the concentration of Co increased, while the Raman spectral line at 260 and 720 cm^{-1} showed a red shift and the Raman spectral line at 305 cm^{-1} showed a blue shift. The blue shift of E (TO) mode could be due to an increase in tensile stress
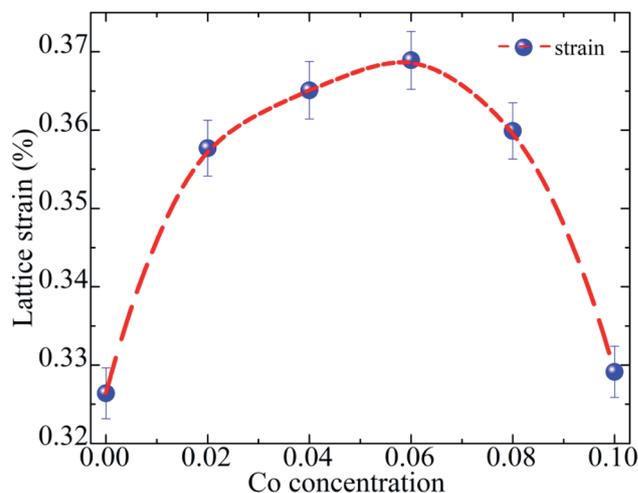

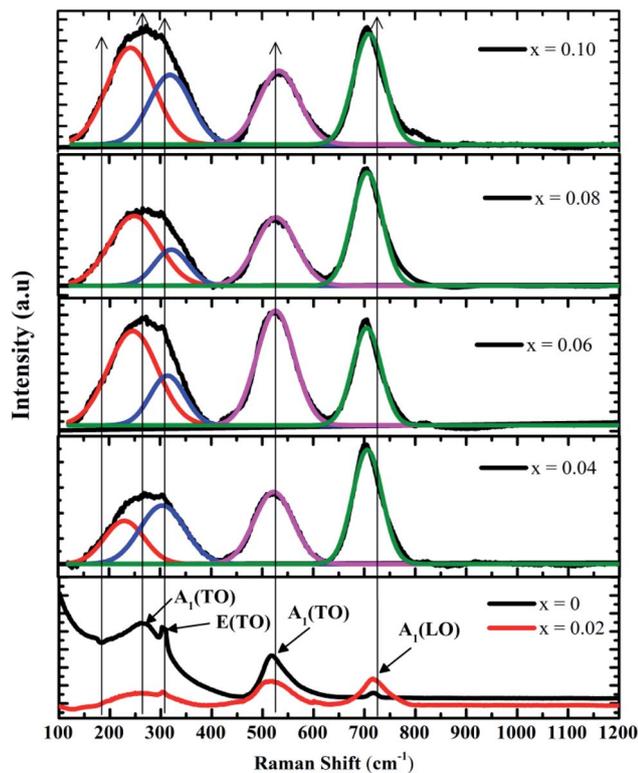**Fig. 2** Variation in lattice microstrain as a function Co composition.

Fig. 3 Room-temperature Raman spectra of $BaTi_{1-x}Co_xO_3$ samples ($0 \leq x \leq 0.10$) and the evolution of the spectra for $x = 0.04, 0.06, 0.08$, and 0.10 samples.

caused by mechanical activation.[37,39] This assumption is not only in accordance with the higher values of microstrain in the samples but is also in agreement with the results of other investigations, in which the shift of the phonon frequencies toward higher values is explained as a result of the rise of tensile type of stress.[37,39] The red shift of the Raman spectral line at 260 and 720 cm^{-1} was observed in $BaTiO_3$ nanoparticles only and was due to the phonon confinement effect of the nanoparticles.[40] However, the crystallite size of the $BaTi_{1-x}Co_xO_3$ compound from XRD is far beyond nano regime. Thus, the red shift of these peaks could be mainly due to the influence of the tensile/compressive nature of stress on $BaTi_{1-x}Co_xO_3$ ceramics.[37]

The Raman analyses proved that the $BaTi_{1-x}Co_xO_3$ samples belong to the tetragonal phase with $P4mm$ symmetry. This result is consistent with the Rietveld refinement of the XRD pattern.

3.3 SEM and EDX studies

Fig. 4 illustrates the representative FESEM micrographs of the samples ($x = 0, x = 0.04$, and $x = 0.1$). The grains have almost uniform polyhedral morphology and are relatively dense with grain size of ~1 μm. The SEM images indicate that all samples have a narrow size distribution due to agglomeration. As shown in Fig. 4, the $x = 0.04$ and $x = 0.1$ samples show a most dense microstructure. This can be elucidated by the fact that Co addition improves the sintering performance, and greatly supports in densification of the $BaTi_{1-x}Co_xO_3$ ceramics. Since

the ionic radii of Ti^{4+} ion is smaller than that of Co^{2+} ion, the substitution of Co^{2+} for Ti^{4+} leads to the widening of the lattice of the $BaTi_{1-x}Co_xO_3$ ceramic. Consequently, lattice distortion improves sintering, and also accelerates the solidification of ceramics. The elemental compositions of the fabricated samples were analyzed by EDX (inset of Fig. 4). The spectrum was used to detect the presence of all chemical elements for $x = 0, x = 0.04$, and $x = 0.1$ samples. In pure $BaTiO_3$ ceramic, the quantitative analysis indicates that the atomic ratio of Ba, Ti, and O is about $1 : 1 : 3$. In the Co-doped samples, the measured atomic percentages of each element detected by EDX analysis are slightly lower than the theoretical values during synthesis (inset of Fig. 4). The EDX results overall confirm the successful Co substitution in $BaTi_{1-x}Co_xO_3$ ceramics.

3.4 UV-visible spectroscopic studies

The optical properties of $BaTi_{1-x}Co_xO_3$ ceramics were studied through UV-visible absorption measurement. Fig. 5 shows UV-Vis spectrum of all samples within 300–600 nm wavelength at room temperature. The absorption edge shifts toward a shorter wavelength region as the concentration of the Co ion increases. This shift can be due to the charge transfer from the valence band to the conduction band. Furthermore, no other absorption was recorded in the far visible region. The direct band gap energy of the synthesized $BaTi_{1-x}Co_xO_3$ ceramics was determined from the absorbance spectra and calculated by Tauc's equation as follows:

$$(\alpha h\nu)^2 = A(h\nu - E_g) \tag{2}$$

where α is the absorption coefficient, $h\nu$ is the identical energy of corresponding wavelength, A is a constant, and E_g is the direct band gap. Fig. 6 plots the value of $(\alpha h\nu)^2$ *versus* photon energy ($h\nu$) for different Co concentrations. The absorption edge is fitted by a straight line, and the intercept of the straight line with the photon energy axis yields the value of the band gap. The direct band gap of each sample are 3.14, 3.25, 3.27, 3.29, 3.33, and 3.44 eV for 0, 2, 4, 6, 8, and 10 at% Co-doped $BaTiO_3$ ceramics, respectively. The band gap of the pure sample ($BaTiO_3$) is 3.14 eV, with matches well with the value in the literature.[41,42] Variation in the band gap energy with increasing doping concentration are presented in Table 2. In the pure $BaTiO_3$, the energy band gap is determined by the difference between the conduction band, mainly composed of Ti 3d orbitals and the valence band, mainly made up of O 2p orbitals. Therefore, the impurity states due to oxygen vacancies and 3d Co doping levels play an important role in the formation of the band structure, with the introduction of localized bands within the original band gap of BTO crystal. As a result, the optical band gap in the Co-doped $BaTiO_3$ can be smaller than that of the pure $BaTiO_3$ crystal.

In our case, the widening in the optical band gap energy is attributed to the Burstein–Moss effect[43] rather than the impact of the oxygen vacancies on the 4d and 2p states of the nearest titanium and oxygen ions. In a p-type semiconductor-liked, the Co doped $BaTiO_3$, the Fermi energy level lies close to the valence band. As the hole concentration increases, the position of Fermi
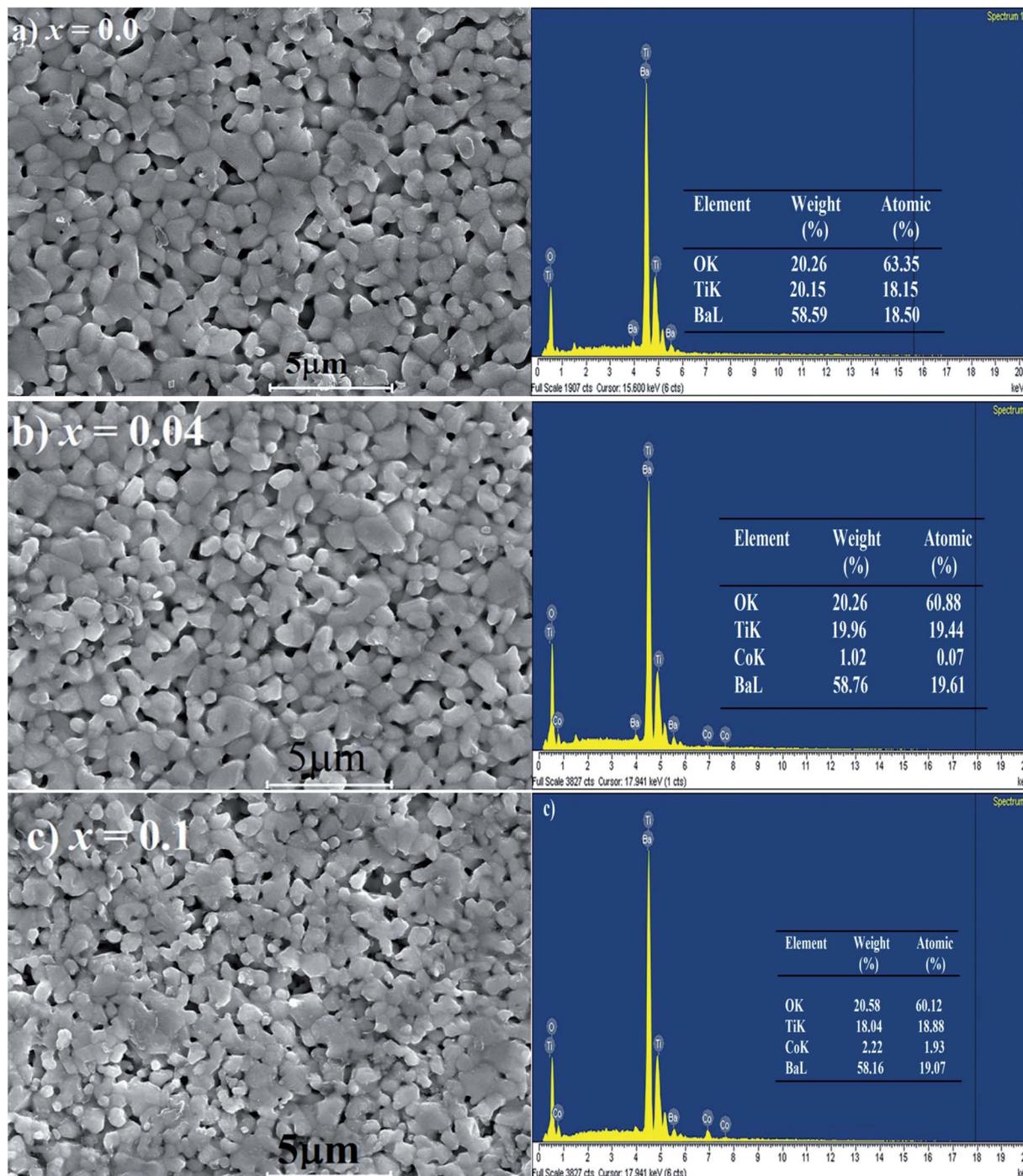
Fig. 4 Scanning electron microscope (SEM) micrographs of $BaTi_{1-x}Co_xO_3$: (a) $x = 0$, (b) $x = 0.04$, (c) $x = 0.1$, with their EDX patterns. Inset: weight % and atomic % of chemical elements in the samples.

level gets disturbed and shifted within the valence band. Due to the incorporation of holes or a vacant energy state, the electrons in the valence band make a transition to occupy the available states. This transition and the gradual addition of holes make the Fermi level to shift further below the valence band and thus the band gap is widened as increasing Co concentration, which may also explain the appearance of the blue shift in Co doped $BaTiO_3$.

3.5 Dielectric constant study

Dielectric constant is calculated using the following equations:

$$\varepsilon' = \frac{Z''}{\omega C_0 \left(Z'^2 + Z''^2 \right)} \tag{3}$$
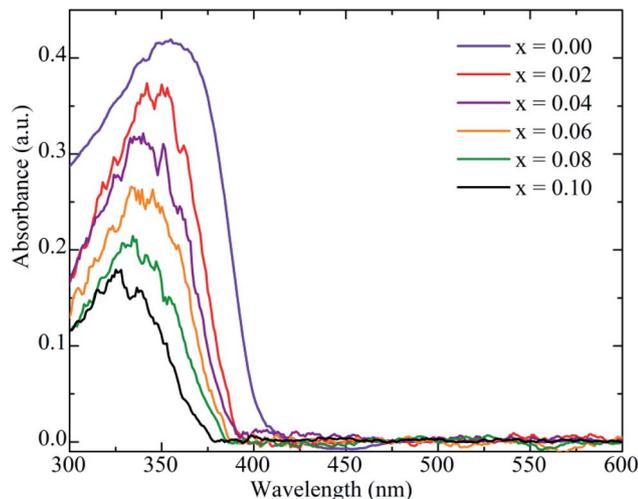
Fig. 5 Optical absorption spectra of $BaTi_{1-x}Co_xO_3$ samples ($0 \leq x \leq 0.10$).

Table 2 Calculated values of frequency exponent s, exponent β, maximum barrier height (W_M), and optical band gap (E_g^{opt}) for $BaTi_{1-x}Co_xO_3$ compounds

Sample	s	β	W_M (eV) calculated by eqn (10)	E_g^{opt} (eV)
$x = 0$	0.797	0.203	0.76	3.14
$x = 0.02$	0.806	0.194	0.80	3.25
$x = 0.04$	0.807	0.193	0.81	3.27
$x = 0.06$	0.810	0.190	0.82	3.29
$x = 0.08$	0.812	0.188	0.83	3.33
$x = 0.1$	0.822	0.178	0.87	3.44

$$\varepsilon'' = \frac{Z'}{\omega C_0 \left(Z'^2 + Z''^2 \right)} \tag{4}$$

in which $\omega = 2\pi f$ is the angular frequency, C_0 is the geometrical capacitance of the empty cell calculated using the following equation: $C_0 = \varepsilon_0 A/t$, where ε_0 is the permittivity of vacuum (8.854×10^{-12} F m^{-1}), A is the surface area, t is the thickness of the sample, and Z' and Z'' are real and imaginary parts of complex impedance, respectively.

Fig. 7 shows the variations in the real (ε') and imaginary (ε'') parts of dielectric constant (ε) for $BaTi_{1-x}Co_xO_3$ ceramics as a function of frequency. The ε' and ε'' profiles of each sample increase at low frequency and decrease at high frequency. The considerable drop in the value of the dielectric constant of each sample at higher frequencies might be due to the interfacial polarization of the grains.[44] This behavior occurs in dielectric ceramic materials. The phenomenon of dielectric constant in $BaTi_{1-x}Co_xO_3$ ceramics has be known as a dispersion, which was characterized by the Maxwell–Wagner-type interfacial polarization governed with Koop's theory.[45,46] This behavior is well explained by the Maxwell–Wagner type relaxation that often occurs in heterogeneous systems with different conductivity types.[47] According to this model, polycrystalline ceramics have

a heterogeneous microstructure that consists of perfectly conducting grains separated by insulating grain boundaries. The AC conductivity measurements further provide evidence of Maxwell–Wagner relaxation. Moreover, real (ε') and imaginary (ε'') parts of the dielectric constant decreases with increasing Co doping level. The large dielectric constant at lower frequencies of Co-doped $BaTiO_3$ ceramic samples is comparable with the values in many advanced ferroelectric materials.[48,49]

3.6 Conductivity mechanism study

The AC conductivity (σ_{ac}) of Co-doped $BaTiO_3$ ceramics was analyzed to obtain insights regarding the conductivity mechanism involved in the system. AC conductivity (σ_{ac}) can be determined from the dielectric data by the following equation:

$$\sigma_{ac} = 2\pi f \varepsilon_0 \varepsilon'' \tag{5}$$

where f is the frequency (Hz), ε_0 is the permittivity of vacuum, and ε'' is the imaginary part of dielectric permittivity.

Fig. 8 displays the frequency dependence of the ac conductivity for all samples. Three distinct regions appear within the measured frequency (insert of Fig. 8): (i) plateau region at low frequencies ($f < 10^2$ Hz), which indicates that the dc conductivity consists of the total conductivity of the grain boundary-grain, (ii) the first dispersion region at intermediate frequencies ($f \sim 10^2$–10^4 Hz) due to the trapped charges between grains, and (iii) the second dispersion region at higher frequencies ($f > 10^4$ Hz), corresponding to the tremendous increase in the mobility of charge carriers in the materials.[50] In this region, the conductivity behavior is described by the Jonscher's power law:

$$\sigma_{ac} = \sigma_{dc} + A\omega^s \tag{6}$$

where σ_{ac} is the ac conductivity, σ_{dc} is the dc conductivity (the frequency independent conductivity), A is a pre-exponential constant, $\omega = 2\pi f$ is the angular frequency, and s is the power law exponent, where $0 < s < 1$. A change in conductive characteristic of the material from low frequency to high frequency as above-mentioned could be attributed the transition from long-range hopping to short-range ionic motion and can be interpreted based on the jump relaxation model (JRM) proposed by Funke and conduction through grain boundaries.[51,52] The frequency-independent plateau at low frequencies is attributed to a successful hopping of charged species to the neighboring available site. The conductivity at high frequencies is a result of the competition of two relaxation processes: (i) unsuccessful hopping from the correlated forward and backward motion of these ions; and (ii) successful hopping after the ions move to the new site and obtain sufficient time to relax. The higher increase in the ratio of successful to unsuccessful hoping rate leads to more dispersive behavior in ac conductivity at high frequencies. Moreover, the ac conductivity increased with increasing Co content in the compound. Hence, within the framework of JRM, the conductivity mechanism in different frequency regions can be explained using a double power law:[51,52]

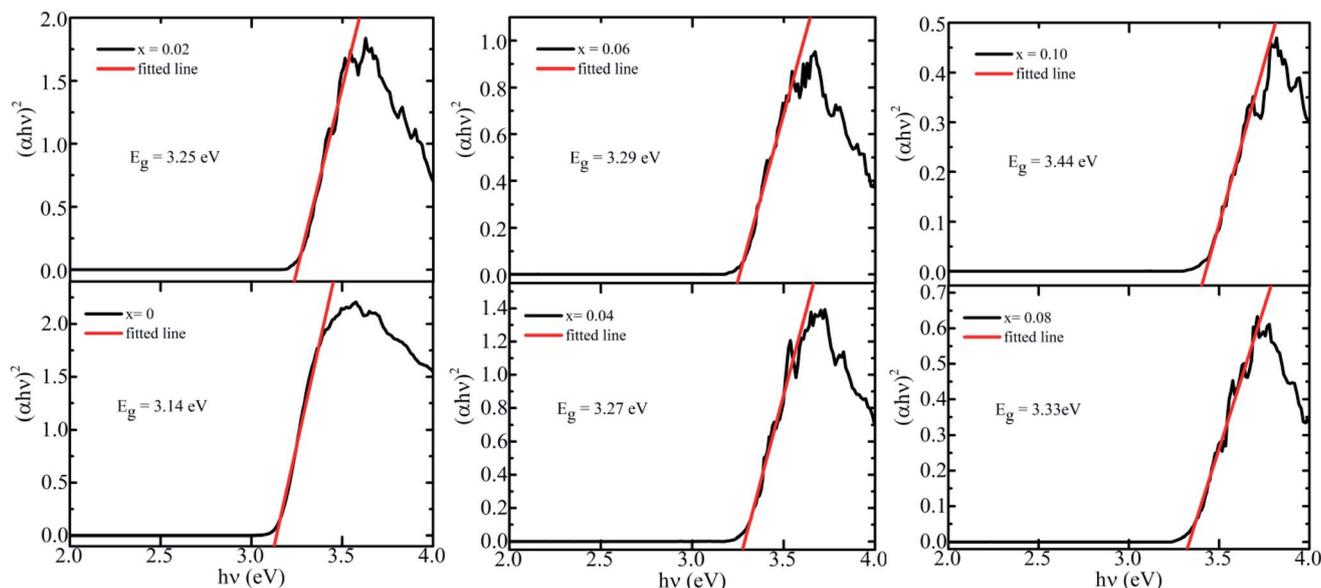$$\sigma_{ac} = \sigma_{dc} + A_1 \omega^{s_1} + A_2 \omega^{s_2} \tag{7}$$

Fig. 6 Dependence of $(\alpha h\nu)^2$ of $BaTi_{1-x}Co_xO_3$ ceramics ($0 \le x \le 0.10$) on incident photon energy ($h\nu$).

where A_1, A_2, s_1, and s_2 are constants depending on the material property. The σ_{dc} term corresponds to the long-range translational hopping in the long-term limit, which is contributed by dc conductivity. The second term $A_1\omega^{s_1}$ with exponent $0 < s_1 < 1$ corresponds to the low frequency dispersion attributed to the short-range translational hopping. The third term $A_2\omega^{s_2}$ with exponent $0 < s_2 < 2$ represents the dispersion at high frequencies due to localized or re-orientational hopping motion.[53] The values of s_1 and s_2 were obtained by fitting the data in Fig. 8 (solid lines) and found to be less than unity. Similar results of s_1 and s_2 were reported by Sharma *et al.*[54] for $BaTiO_3$–$CoFe_{1.8}$-$Zn_{0.2}O_4$ multiferroic particulate composites. Our result indicates that the conductivity at low frequencies may be attributed to the short-range transnational hopping and the conductivity at higher frequencies may be due to localized reorientation

arising to hopping between adjacent lattice sites.[55] The charge carriers (*i.e.* polarons, electrons, or ions) are responsible for the conduction mechanism. Therefore, four models can define the conduction mechanism:[56] (i) the correlated barrier hopping (CBH), (ii) the non-overlapping small polaron tunneling (NSPT), (iii) the overlapping large polaron tunneling (OLPT), and (iv) the quantum mechanical tunneling (QMT) models. The CBH model proposed by Elliott[57] has been applied to interpret the conductivity mechanism in semiconductor materials. According to this model, the charge carries hop over the coulombic barriers that separate them. The relationship between exponent s and barrier height (W) is given by:

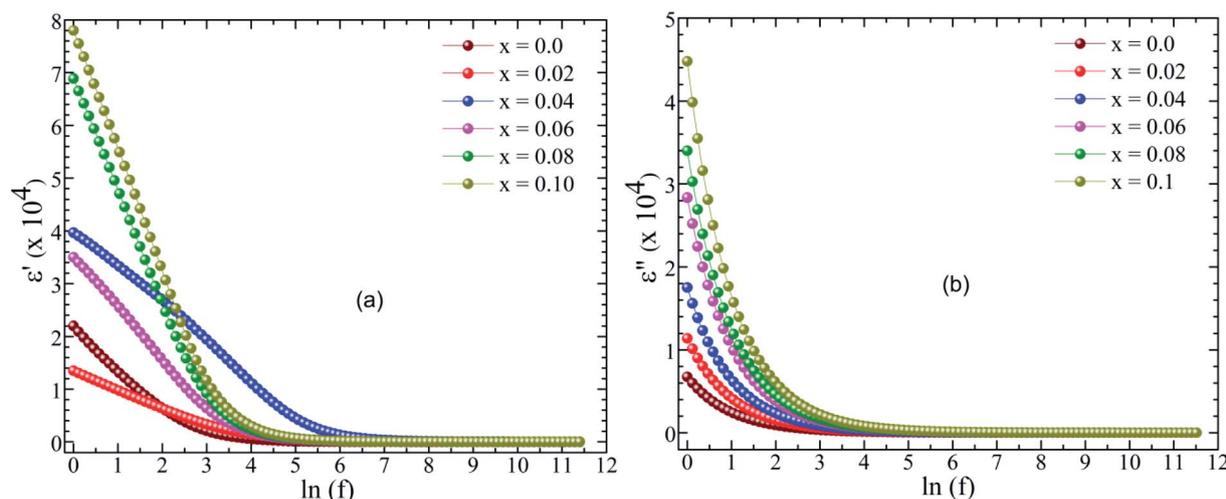$$s = 1 - \frac{6k_BT}{W_M + [k_BT \ln(\omega\tau_0)]} \quad (8)$$

Fig. 7 Frequency dependence of real (ε') (a) and imaginary (ε'') dielectric constants in $BaTi_{1-x}Co_xO_3$ samples ($0 \le x \le 0.10$) ceramics.
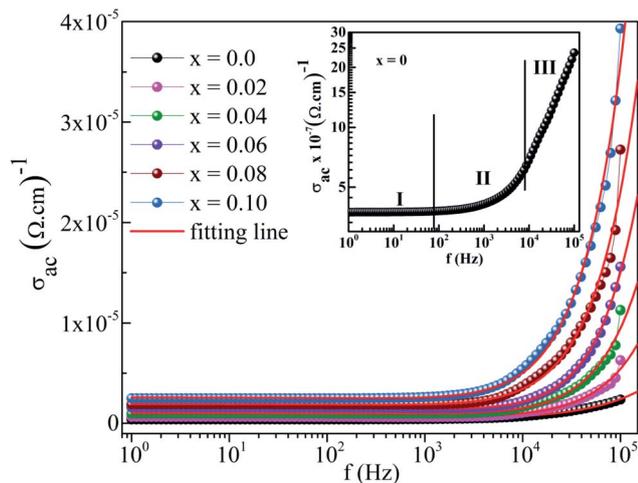
Fig. 8 Plot of AC conductivity against frequency of $BaTi_{1-x}Co_xO_3$ ceramics. The double power law fits are shown as continuous lines. The inset shows the AC conductivity of $x = 0$ sample with three different regions.

where τ_0 is the characteristic relaxation time, and W_M is the maximum height of the energy band necessary to move a charge carrier from one site to another.

In the case of $W_M \gg k_BT$, eqn (8) can be written as:

$$s = 1 - \frac{6k_BT}{W_M} \tag{9}$$

or

$$\beta = 1 - s = \frac{6k_BT}{W_M} \tag{10}$$

W_M is related to the optical band gap (E_g) of the material. When W_M is equal to the optical band gap ($W_M = E_g$), the hopping species are bipolarons.[57] When W_M is a quarter of the optical band gap ($W_M = E_g/4$), single-polaron hopping is the dominant conduction mechanism.[58] The calculated values of s, β, and W_M are listed in Table 2. The frequency exponent s slightly increases with increasing concentration of Co in the samples, and W_M is approximately a quarter of the optical band gap of BTCO ceramics at room temperature, (*i.e.* $T = 300$ K). Hence, single-polaron hopping is the dominant conduction mechanism in BTCO ceramics. The polaron hopping conduction mechanism in 5 at% Co doped h-BaTiO$_3$ was also reported by Wang *et al.*[59]

3.7 Cole–Cole plot studies

Cole–Cole plots are the most relevant tool to investigate the contribution of microscopic electric properties such as grain, grain boundaries, and interface, to the electrical behavior of the material.[60] Fig. 9 shows the Cole–Cole plot of the real (Z') part *versus* imaginary (Z'') part of all samples at room temperature. The plot of the $x = 0$ sample represents two semicircles, suggesting the existence of bulk and grain boundary effects in the sample. By contrast, the single semicircle in the doped samples indicates that the grain or bulk effect is dominant over grain resistance. The Cole–Cole plots were fitted using the commercially available software ZSimpWin by choosing the appropriate equivalent circuit. The two semicircles in the $x = 0$ sample were modeled by a parallel combination of (i) bulk resistance (R_g) and a constant phase element (CPE) with a parallel combination of (ii) grain boundary resistance (R_{gb}), grain boundary capacitance (C_{gb}) and a constant phase element (CPE). For the
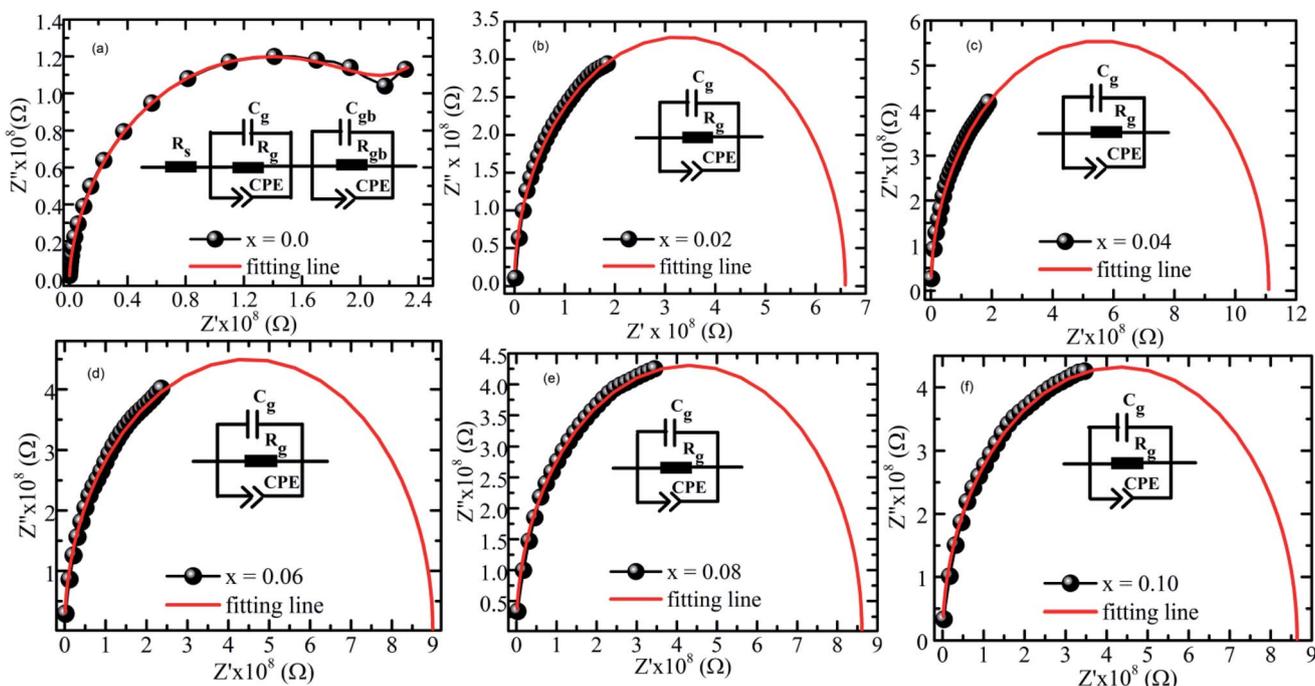

Fig. 9 Fitting lines and Cole–Cole plots of real (Z') and imaginary (Z'') parts of complex impedance in $BaTi_{1-x}Co_xO_3$ ceramics.

remaining samples, the single semicircular arc was fitted using the equivalent circuit, that is, the parallel combination of (i) bulk resistance (R_g), bulk capacitance (C_g), and CPE. A close agreement between the experimental data and fitted value was observed, suggesting the correctness of selecting the equivalent circuit. The Cole–Cole plots show that the semicircular arcs are depressed, and the center of the arcs lies below the real (Z') axis, suggesting multi-dispersive non-Debye relation. This finding indicates the presence of distributed relaxation time originating from various interacting dipoles or inhomogeneity in the samples.[61]

4. Conclusion

The structural, optical, impedance, and conductivity properties of BaTi$_{1-x}$Co$_x$O$_3$ ($0.0 \leq x \leq 0.1$) ceramics were analyzed. The XRD and Raman-based structural analyses demonstrated the existence of a tetragonal perovskite structure in all prepared samples. The UV-Vis results confirmed the blue shift correspondingly the increase of Co concentration and the change of the direct band gap from 3.14 eV to 3.44 eV. According to the double power law, the frequency response in the conductivity spectra with three regions in the measurement range was proved. The low-frequency conductivity is due to long-range translational hopping, the intermediate-frequency conductivity is attributed to short-range translational hopping, and the high-frequency conductivity is a result of localized or re-orientational hopping motion. The relationship between barrier height and optical band gap demonstrated the single-polaron state of the hopping process. The Cole–Cole plots evidenced the presence of grain and grain boundary contribution in pure sample (BaTiO$_3$), whereas the contribution of grain effect was also demonstrated to be dominant in the doped samples. A suitable equivalent circuit was proposed to fit the experimental data in order to explain the electrical response of the materials. The obtained result proved poly-dispersive relaxation and departure from Debye relaxation process in the samples.

Conflicts of interest

There are no conflicts to declare.

Acknowledgements

P. T. Phong and L. H. Nguyen would like to express our gratitude to the Van Lang University.

References

1 W. Maison, R. Kleeberg, R. B. Heimann and S. Phanichphant, Phase content, tetragonality, and crystallite size of nanoscaled barium titanate synthesized by the catecholate process: effect of calcination temperature, *J. Eur. Ceram. Soc.*, 2003, **23**, 127–132, DOI: 10.1016/S0955-2219(02)00071-7.

2 P. L. Campos, D. E. Diaz-Droguett, R. Lavín and S. Fuentes, Synthesis and structural analysis of Co-doped BaTiO$_3$, *J. Mol. Struct.*, 2015, **1099**, 502–509, DOI: 10.1016/j.molstruc.2015.07.012.

3 M. Fiebig and N. A. Spaldin, Current trends of the magnetoelectric effect, *Eur. Phys. J. B*, 2009, **71**, 293, DOI: 10.1140/epjb/e2009-00266-4.

4 L. L. Hench and L. K. West, *Principles of Electronic Ceramics*, John Wiley & Sons, Inc., 1990, pp. 244–247.

5 A. von Hippel, *Dielectric materials and applications*. New York, Wiley, 1954.

6 G. Schileo, L. Luisman, A. Feteira, M. Deluca and K. Reichmann, Structure-property relationships in BaTiO$_3$–BiFeO$_3$–BiYbO$_3$ ceramics, *J. Eur. Ceram. Soc.*, 2013, **33**, 1457–1468, DOI: 10.1016/j.jeurceramsoc.2013.01.011.

7 H. Nakayama and H. Katayama-Yoshida, Theoretical Prediction of Magnetic Properties of Ba(Ti$_{1-x}$M$_x$)O$_3$ (M=Sc,V,Cr,Mn,Fe,Co,Ni,Cu), *Jpn. J. Appl. Phys.*, 2001, **40**, L1355–L1358, DOI: 10.1143/JJAP.40.L1355.

8 L. Yang, H. Qiu, L. Pan, Z. Guo, M. Xu, J. Yin and X. Zhao, Magnetic properties of BaTiO$_3$ and BaTi$_{1-x}$M$_x$O$_3$ (M=Co, Fe) nanocrystals by hydrothermal method, *J. Magn. Magn. Mater.*, 2014, **350**, 1–5, DOI: 10.1016/j.jmmm.2013.09.036.

9 H. Liu, B. Cao and C. J. O'connor, Structural and magnetic properties of single-crystalline Co-doped barium titanate nanoparticles, *J. Magn. Magn. Mater.*, 2010, **322**, 790–793, DOI: 10.1016/j.jmmm.2009.11.004.

10 T.-L. Phan, P. D. Thang, T. A. Ho, T. V. Manh, T. D. Thanh, V. D. Lam, N. T. Dang and S. C. Yu, Local geometric and electronic structures and origin of magnetism in Co-doped BaTiO$_3$ multiferroics, *J. Appl. Phys.*, 2015, **117**, 17D904, DOI: 10.1063/1.4907182.

11 L. B. Luo, Y. G. Zhao, H. F. Tian, J. J. Yang, J. Q. Li, J. J. Ding, B. He, S. Q. Wei and C. Gao, Ferromagnetism and exchange bias in a diluted magnetic ferroelectric oxide, *Phys. Rev. B*, 2009, **79**, 115210, DOI: 10.1103/PhysRevB.79.115210.

12 Y. Lin, S. Zhang, C. Deng, Y. Zhang, X. Wang and C. Nan, Magnetic behavior and thickness dependence in Co-doped BaTiO$_3$ thin films, *Appl. Phys. Lett.*, 2008, **92**, 112501, DOI: 10.1063/1.2898525.

13 J. M. D. Coey, d^0 ferromagnetism, *Solid State Sci.*, 2005, **7**, 660–667, DOI: 10.1016/j.solidstatesciences.2004.11.012.

14 P. Esther Rubavathi, M. T. Rahul, N. Kalarikkal, G. Das Adhikary and B. Sundarakannan, Enrichment of magnetoelectric effect in the hexagonal BaTi$_{1-x}$Co$_x$O$_3$ artificial type-II multiferroics by defects, *J. Magn. Magn. Mater.*, 2021, **350**, 167927, DOI: 10.1016/j.jmmm.2021.167927.

15 Y. Li, Q. Liu, T. Yao, Z. Pan, Z. Sun, Y. Jiang, H. Zhang, Z. Pan, W. Yan and S. Wei, Hexagonal BaTi$_{1-x}$Co$_x$O$_3$ phase stabilized by Co dopants, *Appl. Phys. Lett.*, 2010, **96**, 091905, DOI: 10.1063/1.3337110.

16 S.-W. Yu, W.-C. Vincent Yeh, J.-L. Jou and C.-M. Lei, Synthesis and Characterization the Dielectric Properties of Cobalt Doping Hexagonal BaTiO$_3$, *Ferroelectrics*, 2013, **456**, 31–37, DOI: 10.1080/00150193.2013.846190.

17 X. K. Wei, Q. H. Zhang, F. Y. Li, C. Q. Jin and R. C. Yu, Structural evolution induced by acceptor doping into BaTiO₃ ceramics, *J. Alloys Compd.*, 2010, **508**, 486–493, DOI: 10.1016/j.jallcom.2010.08.099.

18 G. M. Keith, M. J. Rampling, K. Sarma, N. Mc. Alford and D. C. Sinclair, Synthesis and characterisation of doped 6H-BaTiO₃ ceramics, *J. Eur. Ceram. Soc.*, 2004, **24**, 1721–1724, DOI: 10.1016/S0955-2219(03)00495-3.

19 A. Kumar, B. Poojitha, A. Rathore and S. Saha, Structural and magnetic properties of transition metal doped BaTiO₃, *AIP Conf. Proc.*, 2020, **2265**, 030567, DOI: 10.1063/5.0016737.

20 H. Liu, C. Hu and Z. L. Wang, Composite-Hydroxide-Mediated Approach for the Synthesis of Nanostructures of Complex Functional-Oxides, *Nano Lett.*, 2006, **6**, 1535–1540, DOI: 10.1021/nl061253e.

21 Y.-F. Zhu, L. Zhang, T. Natsuki, Y.-Q. Fu and Q.-Q. Ni, Facile Synthesis of BaTiO₃ Nanotubes and Their Microwave Absorption Properties, *ACS Appl. Mater. Interfaces*, 2012, **4**, 2101–2106, DOI: 10.1021/am300069x.

22 T. Sahoo, S. K. Tripathy, M. Mohapatra, S. Anand and R. P. Das, X-ray diffraction and microstructural studies on hydrothermally synthesized cubic barium titanate from TiO₂–Ba(OH)₂–H₂O system, *Mater. Lett.*, 2007, **61**, 1323–1327, DOI: 10.1016/j.matlet.2006.07.025.

23 W. J. Dawson, Hydrothermal Synthesis of Advanced Ceramic Powder, *Am. Ceram. Soc. Bull.*, 1988, **67**, 1673–1678.

24 W. Zhu, S. A. Akbar, R. Asiaie and P. K. Dutta, Sintering and Dielectric Properties of Hydrothermally Synthesized Cubic and Tetragonal BaTiO₃ Powders, *Jpn. J. Appl. Phys.*, 1997, **36**, 214, DOI: 10.1143/JJAP.36.214.

25 S. El Kossi, J. Dhahria and E. K. Hlilb, Structural, magnetic and theoretical investigations on the magnetocaloric properties of La$_{0.7}$Sr$_{0.25}$K$_{0.05}$MnO₃ perovskite, *RSC Adv.*, 2016, **6**, 63497–63507, DOI: 10.1039/C6RA08642J.

26 D. B. Wiles and R. A. Young, A new computer program for Rietveld analysis of X-ray powder diffraction patterns, *J. Appl. Crystallogr.*, 1981, **14**, 149–151, DOI: 10.1107/S0021889881008996.

27 A. Rani, J. Kolte and P. Gopalan, Structural, electrical, magnetic and magnetoelectric properties of Co-doped BaTiO₃ multiferroic ceramics, *Ceram. Int.*, 2018, **44**, 16703–16711, DOI: 10.1016/j.ceramint.2018.06.098.

28 R. H. Buttner and E. N. Maslen, Structural parameters and electron difference density in BaTiO₃, *Acta Crystallogr. B*, 1992, **48**, 764–769, DOI: 10.1107/S010876819200510X.

29 L. P. Campos, D. E. Diaz-Droguett, R. Lavín and S. Fuentes, Synthesis and structural analysis of Co-doped BaTiO₃, *J. Mol. Struct.*, 2015, **1099**, 502–509, DOI: 10.1016/j.molstruc.2015.07.012.

30 D. K. Pradhan, H. S. Mohanty, S. Kumari, K. B. N. Tang, Ravikant, M. M. Rahaman, D. K. Pradhan, A. Kumar, D. A. Gilbertah and P. D. Rack, Ferroic phase transitions and magnetoelectric coupling in cobalt doped BaTiO₃, *J. Mater. Chem. C*, 2021, **9**, 12694–12711, DOI: 10.1039/D1TC02961D.

31 R. D. Shannon, Revised effective ionic radii and systematic studies of interatomic distances in halides and chalcogenides, *Acta Crystallogr., Sect. A: Cryst. Phys., Diffr., Theor. Gen. Crystallogr.*, 1976, **32**, 751–767, DOI: 10.1107/S0567739476001551.

32 Y. Ma, H. Chen, F. Pan, Z. Chen, Z. Ma, X. Lin, F. Zheng and X. Ma, Electronic structures and optical properties of Fe/Co-doped cubic BaTiO₃ ceramics, *Ceram. Int.*, 2019, **45**, 6303–6311, DOI: 10.1016/j.ceramint.2018.12.113.

33 G. Koster, L. Klein, W. Siemons, G. Rijnders, J. S. Dodge, C. B. Eom, D. H. A. Blank and M. R. Beasley, Structure, physical properties, and applications of SrRuO₃ thin films, *Rev. Mod. Phys.*, 2012, **84**, 253, DOI: 10.1103/RevModPhys.84.253.

34 G. K. Williamson and W. H. Hall, X-ray line broadening from filed aluminium and wolfram, *Acta Metall.*, 1953, **1**, 22–31, DOI: 10.1016/0001-6160(53)90006-6.

35 X. Tian, J. Li, K. Chen, J. Han and S. Pan, Nearly Monodisperse Ferroelectric BaTiO₃ Hollow Nanoparticles: Size-Related Solid Evacuation in Ostwald-Ripening-Induced Hollowing Process, *Cryst. Growth Des.*, 2010, **10**, 3990–3995, DOI: 10.1021/cg1005727.

36 A. Scalabrin, A. S. Chaves, D. S. Shim and S. P. S. Porto, Temperature dependence of the A₁ and E optical phonons in BaTiO₃, *Phys. Status Solidi B*, 1977, **79**, 731–742, DOI: 10.1002/pssb.2220790240.

37 V. P. Pavlovic, M. V. Nikolic, V. B. Pavlovic, J. Blanusa, S. Stevanovic, V. V. Mitic, M. Scepanovic, B. Vlahovic and M. Hoffman, Raman Responses in Mechanically Activated BaTiO₃, *J. Am. Ceram. Soc.*, 2014, **97**, 601–608, DOI: 10.1111/jace.12423.

38 F. A. Rabuffetti and R. L. Brutchey, Structural Evolution of BaTiO₃ Nanocrystals Synthesized at Room Temperature, *J. Am. Chem. Soc.*, 2012, **134**, 9475–9487, DOI: 10.1021/ja303184w.

39 M. S. Chen, Y. X. Shen, S. H. Tang, W. S. Shi, D. F. Cui and Z. H. Chen, Stress effect on Raman spectra of Ce-doped BaTiO₃ films, *J. Phys.: Condens. Matter*, 2000, **12**, 7013, DOI: 10.1088/0953-8984/12/31/303.

40 S. Ramakanth and K. C. James Raju, Band gap narrowing in BaTiO₃ nanoparticles facilitated by multiple mechanisms, *J. Appl. Phys.*, 2014, **115**, 173507, DOI: 10.1063/1.4871776.

41 N. V. Dang, T.-L. Phan, T. D. Thanh, V. D. Lam and L. V. Hong, Structural phase separation and optical and magnetic properties of BaTi$_{1-x}$Mn$_x$O₃ multiferroics, *J. Appl. Phys.*, 2012, **111**, 113913, DOI: 10.1063/1.4725195.

42 P. T. Phong, L. T. H. Phong, N. V. Dang, D. H. Manh and I.-J. Lee, Structural, optical and conductivity properties of BaTi$_{1-x}$Ni$_x$O₃, *Ceram. Int.*, 2016, **42**, 7414–7421, DOI: 10.1016/j.ceramint.2016.01.145.

43 P. D. C. King, T. D. Veal, F. Fuchs, C. Y. Wang, D. J. Payne, A. Bourlange, H. Zhang, G. R. Bell, V. Cimalla, O. Ambacher, R. G. Egdell, F. Bechstedt and C. F. Mc Conville, Band gap, electronic structure, and surface electron accumulation of cubic and hombohedral In₂O₃, *Phys. Rev. B*, 2009, **79**, 205211, DOI: 10.1103/PhysRevB.79.205211.

44 M. T. Busacglia, V. Busaglia, M. Viviani, J. Petzelt, M. Savinov, L. Mitoseriu, A. Testino, P. Nanni,

C. Harnagea, Z. Zhao and M. Nygren, Ferroelectric properties of dense nanocrystalline $BaTiO_3$ ceramics, *Nanotechnology*, 2004, **15**, 1113, DOI: **10.1088/0957-4484/15/9/001**.

45 K. W. Wagner, Zur Theorie der unvollkommenen Dielektrika, *Ann. Phys.*, 1913, **345**, 817–855, DOI: **10.1002/andp.19133450502**.

46 C. G. Koops, On the Dispersion of Resistivity and Dielectric Constant of Some Semiconductors at Audiofrequencies, *Phys. Rev.*, 1951, **83**, 121, DOI: **10.1103/PhysRev.83.121**.

47 D. O'Neill, R. M. Bowman and J. M. Gregga, Dielectric enhancement and Maxwell–Wagner effects in ferroelectric superlattice structures, *Appl. Phys. Lett.*, 2000, **77**, 1520, DOI: **10.1063/1.1290691**.

48 Md G. Masud, B. K. Chaudhuri and H. D. Yang, High dielectric permittivity and room temperature magneto-dielectric response of charge disproportionate $La_{0.5}Ba_{0.5}FeO_3$ perovskite, *J. Phys. D: Appl. Phys.*, 2011, **44**, 255403, DOI: **10.1088/0022-3727/44/25/255403**.

49 R. N. Bhowmik, Dielectric and magnetic study of $BaTi_{0.5}Mn_{0.5}O_3$ ceramics, synthesized by solid state sintering, mechanical alloying and chemical routes, *Ceram. Int.*, 2012, **38**, 5069–5080, DOI: **10.1016/j.ceramint.2012.03.009**.

50 L. L. Hench and J. K. West, *Principles of Electronic Ceramics*, Wiley, Singapore, 1990.

51 N. Ortega, A. Kumar, P. Bhattacharya, S. B. Majumder and R. S. Katiyar, Impedance spectroscopy of multiferroic $PbZr_xTi_{1-x}O_3/CoFe_2O_4$ layered thin films, *Phys. Rev. B*, 2008, **77**, 014111, DOI: **10.1103/PhysRevB.77.014111**.

52 S. R. Kanuru, K. Baskar and R. Dhanasekaran, Synthesis, structural, morphological and electrical properties of NBT-BT ceramics for piezoelectric applications, *Ceram. Int.*, 2016, **42**, 6054–6064, DOI: **10.1016/j.ceramint.2015.12.162**.

53 K. Funke, Jump relaxation in solid electrolytes, *Prog. Solid State Chem.*, 1993, **22**, 111–195, DOI: **10.1016/0079-6786(93)90002-9**.

54 R. Sharma, P. Pahuja and R. P. Tandon, Structural, dielectric, ferromagnetic, ferroelectric and ac conductivity studies of the $BaTiO_3$-$CoFe_{1.8}Zn_{0.2}O_4$ multiferroic particulate composites, *Ceram. Int.*, 2014, **40**, 9027–9036, DOI: **10.1016/j.ceramint.2014.01.115**.

55 H. Chen, C. Yang, J. Zhang, B. Wang and H. Ji, Electrical behavior of $BaZr_{0.1}Ti_{0.9}O_3$ and $BaZr_{0.2}Ti_{0.8}O_3$ thin films, *Appl. Surf. Sci.*, 2009, **255**, 4585–4589, DOI: **10.1016/j.apsusc.2008.12.003**.

56 M. Ben Bechir, K. Karoui, M. Tabellout, K. Guidara and A. Ben Rhaiem, Electric and dielectric studies of the $[N(CH_3)_3H]_2CuCl_4$ compound at low temperature, *J. Alloys Compd.*, 2014, **588**, 551–557, DOI: **10.1016/j.jallcom.2013.11.141**.

57 S. R. Elliott, A theory of a.c. conduction in chalcogenide, *Philos. Mag.*, 1977, **36**, 1291–1304, DOI: **10.1080/14786437708238517**.

58 S. R. Elliott, A.c. conduction in amorphous chalcogenide and pnictide semiconductors, *Adv. Phys.*, 1987, **36**, 135–217, DOI: **10.1080/00018738700101971**.

59 J. Wang, H. Zhang, D. Xue and Z. Li, Electrical properties of hexagonal $BaTi_{0.8}Co_{0.2}O_{3-\delta}$ ceramic with NTC effect, *J. Phys. D: Appl. Phys.*, 2009, **42**, 235103, DOI: **10.1088/0022-3727/42/23/235103**.

60 P. Gupta, P. K. Mahapatra and R. N. P. Choudhary, Investigation on structural and electrical properties of Co and W modified $BaTiO_3$, *Ceram. Int.*, 2019, **45**, 22862–22871, DOI: **10.1016/j.ceramint.2019.07.329**.

61 M. Rekaby, Dielectric response and Cole–Cole plot analysis for $(Zn_{0.91}Mn_{0.03}Co_{0.06}O)_x/Cu_{0.5}Tl_{0.5}Ba_2Ca_2Cu_3O_{10-\delta}$ diluted magnetic semiconductor/superconductor composites, *Appl. Phys. A*, 2020, **126**, 664, DOI: **10.1007/s00339-020-03849-z**.